APL Materials

RESEARCH ARTICLE | APRIL 10 2026

Anisotropic crystallization of orthorhombic ScSi on Si(001) substrates

Bert Pollefliet ; Clement Porret ; Jean-Luc Everaert ; Kiroubanand Sankaran ; Olivier Richard ; Han Han ; Roger Loo ; Christophe Detavernier ; André Vantomme ; Clement Merckling

APL Mater. 14, 041103 (2026)
https://doi.org/10.1063/5.0326525

Articles You May Be Interested In

Theoretical research on general Hosford yield function of cubic orthorhombic sheets metals

AIP Conf. Proc. (April 2017)

Magnetic hardness of hexagonal and orthorhombic Fe_3C, Co_3C, $(Fe–Co)_3C$, and their alloys with boron, nitrogen, and transition metals: A first-principles study

APL Mater. (February 2025)

Effect of quenching temperature on orthorhombic boride formation at crystallization of amorphous ribbons $Fe_{82}B_{18}$

AIP Conf. Proc. (August 2015)

12 June 2026 12:02:48

Anisotropic crystallization of orthorhombic ScSi on Si(001) substrates

Cite as: APL Mater. 14, 041103 (2026); doi: 10.1063/5.0326525
Submitted: 6 February 2026 • Accepted: 26 March 2026 •
Published Online: 10 April 2026

Bert Pollefliet,[1,2,a)] Clement Porret,[2] Jean-Luc Everaert,[2] Kiroubanand Sankaran,[2] Olivier Richard,[2] Han Han,[2] Roger Loo,[2,3] Christophe Detavernier,[3] André Vantomme,[4] and Clement Merckling[1,2]

AFFILIATIONS

[1] Department of Materials Engineering, KU Leuven, Kasteelpark Arenberg 44, 3001 Leuven, Belgium
[2] imec, Kapeldreef 75, 3001 Leuven, Belgium
[3] Department of Solid State Sciences, Ghent University, Krijgslaan 285, 9000 Gent, Belgium
[4] Quantum Solid State Physics, KU Leuven, Celestijnenlaan 200d, 3001 Leuven, Belgium

[a)] Author to whom correspondence should be addressed: bert.pollefliet@imec.be

ABSTRACT

Scandium-based silicides have attracted attention as new contact materials for ultimately scaled CMOS devices. Excellent contact properties in combination with P-doped Si have been demonstrated. However, unlike conventional Ti, Co, and Ni silicides, little is known about the formation mechanisms and properties of Sc silicides. This manuscript, therefore, reports on the formation and structural properties of orthorhombic ScSi silicide formed by solid state reaction between a sputter deposited 15 nm Sc film and a Si(001) substrate. Synchrotron x-ray diffraction (XRD) pole figures, in combination with cross-sectional transmission electron microscopy, are leveraged to determine the texture of ScSi. An epitaxial texture with two different components is evidenced. Large (≳20 nm) grains, having a minimal defectivity originating from the lattice mismatch between the silicide and the substrate, are distinguished from small (≲5 nm) nanotwinned grains. The formation of these two sets of grains is investigated by *in situ* XRD. Due to a solid state amorphization reaction between Sc and Si, the formation of orthorhombic ScSi is preceded by the formation of an amorphous ScSi phase. Orthorhombic ScSi formation is initiated at ~320 °C by the crystallization of small nuclei at the interface with Si, as evidenced for the first time by cross-sectional transmission electron microscopy. These nuclei share a singular epitaxial orientation, corresponding to the one of the large grains in the final ScSi film. Further crystallization occurs anisotropically in the lateral direction. Along the **c** axis, the initial epitaxial orientation is maintained. However, along the **a** axis, twin defects are generated, resulting in the small grain size.

© 2026 Author(s). All article content, except where otherwise noted, is licensed under a Creative Commons Attribution (CC BY) license (https://creativecommons.org/licenses/by/4.0/). https://doi.org/10.1063/5.0326525

12 June 2026 12:02:48

I. INTRODUCTION

As a result of extreme scaling, the contact resistance R_c between the source/drain (S/D) and metal silicide regions has become the largest component of the switch impedance in modern CMOS devices.[1] The impact of this parasitic resistance can be alleviated by increasing the active contact area A or by lowering the contact specific resistivity ($\rho_c = R_c \cdot A$).[2] The latter requires innovations in materials processing of the S/D, focused on maximizing the active doping concentration, and of the metal silicide, focused on minimizing the Schottky barrier height (SBH).

Given their low SBH compared to conventionally used silicides, such as NiSi, $TiSi_2$, and $CoSi_2$, rare-earth silicides, such as Yb,[3] Er,[4] La,[5] Y,[6] Gd,[7] ternary,[8] and Sc[9] silicides, are good candidates to lower the contact resistivity.[10,11] Thomas *et al.*[12] pioneered the investigation of silicide formation in Sc thin films deposited on Si substrates. Their results show that two different silicides are formed resulting from the solid state reaction between 180 nm thick Sc layers, deposited by vacuum evaporation, and Si(001) substrates. At a temperature of 500 °C, orthorhombic ScSi was reported to be formed by a presumably diffusion controlled silicidation reaction. At higher temperatures (about 900 °C), the nucleation-controlled formation

of hexagonal $ScSi_{1.7}$ was observed. In addition to identifying these phases, electrical measurements on these silicides were conducted. The room temperature resistivity was measured as 21 and 38 $\mu\Omega$ cm for the orthorhombic and hexagonal phases, respectively. Comparing this to C54–$TiSi_2$, $CoSi_2$ or NiSi, for which resistivities as low as 10 $\mu\Omega$ cm were reported,[13–15] it is clear that these silicides are not the most promising in this regard. On the other hand, the SBH on n-Si was reported to be about 0.4 eV, making this an attractive option to lower the contact resistivity in NMOS devices.[9] It should be noted that these studies were done using uncapped samples. Given the strong O gettering properties of the rare-earth metals,[16,17] significant oxidation of the (top part of the) Sc layer is expected to occur post-deposition and/or during annealing in such a case.

In addition to the SBH, the charge carrier effective mass of the metal (silicide) has been identified as a key parameter in maximizing the transmission probability of charge carriers at the metal/semiconductor interface.[18] Dabral *et al.* identified Sc and Y as top candidates due to their high average charge carrier effective mass. Inspired by this, Porret *et al.*[10] demonstrated record low contact resistivities using Sc contacted to highly P-doped Si (Si:P), achieving a ~35% improvement compared to Ti after an isothermal anneal at 420 °C for 20 min. The crystalline and chemical properties of annealed TiN/Sc/Si:P contact stacks were subsequently investigated.[19,20] Crystalline silicide formation was evidenced in the form of orthorhombic ScSi lying atop a thin $Sc_{1-x-y}Si_xP_y$ interfacial layer, which has a commensurate interface with the underlaid Si:P. The excellent contact properties encourage further research on Sc silicide formation. This work, therefore, focuses on the formation and nanostructural properties of orthorhombic ScSi formed via solid state reaction between Sc thin films and Si(001) substrates in annealed TiN/Sc/Si(001).

The texture, i.e., the statistical distribution of grain orientations, can have a profound impact on the formation and stability of silicides, as it controls the type and orientation of grain boundaries and the interface energy. For contact applications, it has been the subject of extensive research as the orientation and size of individual grains will induce local variations in the strain and the SBH, thereby affecting the contact resistivity.[21]

Unlike conventional Ti, Co, and Ni silicides, hardly any information is available on the structural properties of ScSi. In this work, it is shown that ScSi formed on Si(001) is strongly textured, exhibiting two epitaxial texture components. The crystallographic relationship between these two orientations is identified and *in situ* characterization, that is, in real time during annealing, is used to investigate the silicide formation mechanisms. The results confirm a solid state amorphization reaction between the as-deposited Sc and Si, forming amorphous a-ScSi silicide.[19,22,23] Upon further annealing, orthorhombic ScSi nucleates at the interface with Si in a domain matched epitaxial manner.[24] Further crystallization occurs anisotropically, resulting in significant twin defect formation.

II. EXPERIMENTAL METHODS

A. Sample preparation

The contact stack consists of 10 nm TiN/15 nm Sc/Si(001). The Sc and TiN layers are deposited without vacuum break by physical vapor deposition (DC sputtering) using a Canon Anelva system. Both depositions occur at room temperature. This system operates at a base pressure of 10^{-7} Torr. Both sputter processes use Ar as sputter gas, resulting in a pressure of 10^{-4} Torr during processing. For the reactive sputtering of TiN, N_2 gas is used in combination with a Ti target. The deposition rates are 5.2 and 1.5 nm/min for the Sc and TiN layers, respectively. Prior to these depositions, a wet etch in diluted hydrogen fluoride (HF) is performed to minimize the native oxide present on the substrate. Finally, some of the samples are annealed. Two annealing processes are considered: (1) 12 °C/min ramp to 320 °C in N_2(95%)/H_2(5%), followed by an uncontrolled quench to room temperature, and (2) 420 °C anneal for 20 min in N_2(90%)/H_2(10%). The former anneal is conducted using an Anton Paar Domed Hot Stage (DHS) 1100 heating stage, whereas the latter anneal is performed using an A412 ASM furnace and results in the formation of orthorhombic ScSi.[19]

B. Physical characterization

The structural properties of the ScSi thin films are investigated by x-ray diffraction (XRD) pole figures and cross-sectional transmission electron microscopy (TEM). The XRD pole figures are acquired at the Materials Characterisation by X-ray diffraction (MCX) beamline of the Elettra synchrotron in Trieste.[25] The x-ray source is operated with CuK_α photon energy (wavelength λ = 1.5406 Å). The sample is mounted on a four-circle diffractometer and operated in the Bragg–Brentano $\theta/2\theta$ geometry. The setup enables the variation of the sample azimuth (ϕ) and elevation (χ), allowing the collection of pole figures using the Schulz method[26] for ϕ and χ from 0° to 90° in steps of 1°. The fourfold symmetry of the (001)-oriented Si substrate is used to reconstruct the pole figure over the full ϕ range (0°–360°).[27] Finally, the two-dimensional representations are obtained after an equal area projection.[26] The pole figures are plotted with the $(1\bar{1}0)$, (110), $(\bar{1}10)$, and $(\bar{1}\bar{1}0)$ poles of the Si substrate at χ = 90° and ϕ = 0°, 90°, 180°, and 270°, respectively. Following the methodology of De Keyser *et al.*,[27] texture analysis is performed by plotting the parametric equation for alignment between the lattice planes of the silicide ScSi(hkl) and the Si substrate Si(h′k′l′). In this way, the constraint ScSi(hkl)//Si(h′k′l′) is visualized as a pattern of lines on the pole figure. Cross-sectional TEM inspections are performed to investigate the nano-structural properties. These are conducted using a Titan3 G2 60–300 (FEI) system operated at 200 kV. All TEM images are taken along the Si⟨110⟩ zone axis. Complementary energy-dispersive x-ray spectroscopy (EDS) analysis is performed, which confirms the formation of scandium monosilicide after a 420 °C to 20 min anneal (see supplementary material).

In addition to these *ex situ* characterization techniques, *in situ* techniques are used to investigate phase transformations during the solid state reactions. This includes temperature dependent XRD (*in situ* XRD), which records the XRD pattern of a sample as a function of the annealing temperature during a slow temperature ramp (12 °C/min) from room temperature to 900 °C in He(95%)/H_2(5%). These measurements are done using a Bruker D8 diffractometer with a linear (1D) detector with an angular range of 20° in 2θ. During the measurement, the incidence angle of the x-ray source (λ = 1.5406 Å) is fixed at $\omega = \theta$ = 17.5°, and the x-ray intensity is recorded in the 2θ range 25°–45°. This offers limited information for strongly textured films. Hence, in Sec. III D, *in situ* XRD pole figures acquired during annealing are leveraged to obtain a complete view of the sample crystallinity during phase transformations. These measurements

12 June 2026 12:02:48

© Author(s) 2026

are conducted at the DiffAbs beamline of the Synchrotron Soleil[28] using a XPAD S140 area (2D) detector. The x-ray source is operated at an energy of 18 keV (λ = 0.688 804 Å). The optimized approach at DiffAbs allows significantly faster acquisition of pole figures compared to the traditional Schulz approach. Consequently, using an Anton Paar DHS 1100 heating stage, it allows the acquisition of pole figures *in situ* during a slow anneal in N_2(95%)/H_2(5%) consisting of 3 steps: (1) from room temperature to 280 °C at 12 °C/min, (2) from 280 to 380 °C at 1 °C/min, and (3) from 380 to 650 °C at 6 °C/min. The slower ramp rate of step (2) is chosen to increase the temperature resolution during the crystallization of orthorhombic ScSi (orth-ScSi). In addition to the fast acquisition speed, this approach enables the measurement of full pole volumes, covering a range of 2θ values at once.[28] For this work, 2θ from 12° to 22° is used, covering the pertinent orth-ScSi Bragg reflections. This approach also allows for additional flexibility in the data analysis compared to the traditional Schulz method.[29] However, pole figures acquired by this method suffer from additional background scattering due to the use of a graphite dome, which acts as annealing chamber. In addition, due to the presence of the graphite dome, no "laser alignment,"[30] which is used to position the azimuthal rotation axis ϕ perpendicular to the sample surface, can be conducted. This results in a slight non-uniform background in the pole figures.

III. RESULTS

A. Phase sequence of a 15 nm Sc thin film deposited on Si(001) upon annealing

Figure 1 shows the *in situ* XRD pattern of a pristine sample. Four temperature intervals can be identified: (1) <300 °C, (2) 300–400 °C, (3) 400–750 °C, and (4) >750 °C. The as-deposited contact stack contains hexagonal Sc (hex-Sc) with Sc(001)//Si(001) out-of-plane orientation. The formation of a-ScSi as a result of a solid state amorphization (SSA) reaction between Sc and Si has been observed in sputtered Sc/Si multilayers annealed in the 210–250 °C temperature range.[22] In Fig. 1, this SSA reaction is evidenced by a reduction of the Sc(002) peak intensity starting at ~250 °C and results in the full silicidation of Sc at ~300 °C. Upon subsequent annealing, orth-ScSi forms at ~400 °C, yielding the ScSi(040)/(130) peaks. The absence of other Bragg reflections suggests that this phase is strongly textured.[19] Finally, above 750 °C, cubic Sc_2O_3 (cub-Sc_2O_3) forms at the expense of orth-ScSi.

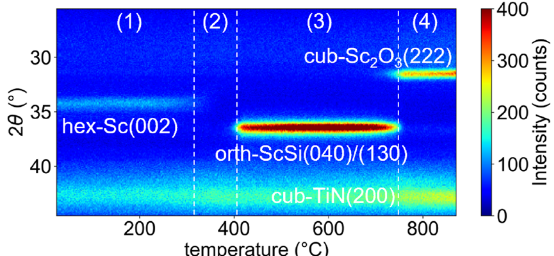

FIG. 1. *In situ* XRD pattern of a 10 nm TiN/15 nm Sc/Si(001) stack measured during a slow temperature ramp of 12 °C/min from room temperature to 900 °C in a He(95%)/H_2(5%) ambient.

B. Texture of orthorhombic ScSi

The *in situ* XRD (Fig. 1) suggests that orth-ScSi has a ScSi(040)/(130)//Si(001) out-of-plane texture. Additional symmetric $2\theta/\theta$ XRD scans reveal that no other peaks are present in the 20°–80° 2θ range (see supplementary material). The texture of

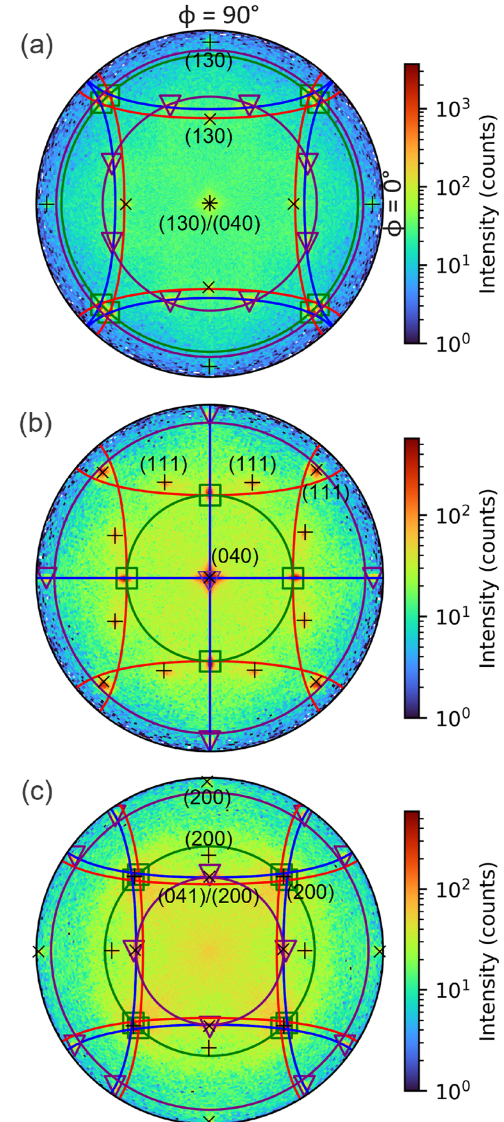

FIG. 2. (a) ScSi(111), (b) ScSi(130), and (c) ScSi(131) XRD pole figures acquired from a 10 nm TiN/15 nm Sc/Si(001) contact stack after 420 °C to 20 min anneal. The calculated line patterns, used to determine the epitaxial orientations, are shown. These patterns were calculated assuming: ScSi(010)//Si(001) (green lines), ScSi(130)//Si(001) (purple lines), ScSi(001)//Si(110) (blue lines), and ScSi(100)//Si(110) (red lines). The resulting epitaxial texture components, detailed in Table I, are indicated by square (□) and triangle (▽) symbols. Note that, due to peak overlap in 2θ, the pole figures contain contributions from neighboring Bragg reflections, which are indexed by cross (×) and plus (+) symbols, corresponding to epitaxy 1 and epitaxy 2 texture components, respectively.

12 June 2026 12:02:48

© Author(s) 2026

TABLE I. Orthorhombic ScSi texture components.

	Out-of-plane alignment	In-plane alignment
Epitaxy 1 (□)	ScSi(010)//Si(001)	ScSi(001)//Si(110) ScSi(100)//Si(110)
Epitaxy 2 (▽)	ScSi(130)//Si(001)	ScSi(001)//Si(110)

orth-ScSi is further investigated using XRD pole figures acquired after a 420 °C to 20 min anneal (Fig. 2).[31] The pole figures contain well-defined spots of high intensity, indicative of an epitaxial texture. The calculated line patterns are included, which are used to determine the epitaxial grain orientations.[27] The resulting texture components are summarized in Table I. Two epitaxial texture components are distinguished. The first component ("*Epi 1*") is characterized by a ScSi(010)//Si(001) out-of-plane and a ScSi(001)//Si(110) in-plane alignment. This orientation also satisfies the ScSi(100)//Si(110) condition. Hence, grains corresponding to this texture component are aligned in-plane with their **a** axis and **c** axis parallel to Si⟨110⟩ at $\chi = 90°$. The second component ("*Epi 2*") also satisfies the ScSi(001)//Si(110) in-plane alignment. The out-of-plane alignment, however, corresponds to an off-normal ScSi(010) fiber texture with the fiber axes at ($\chi \approx 44°$ and $\phi = 0°, 90°, 180°$, or $270°$). This is nearly equivalent to a ScSi(130)//Si(001) out-of-plane alignment, as it can be achieved by tilting the (130) planes by ~4.5° in the direction of the Si(110)-type planes starting from a perfect ScSi(130)//Si(001) out-of-plane orientation, for which the ScSi(010) planes are tilted 39.5° out-of-plane.[32] This small out-of-plane tilt is evidenced by the star-shaped peak in the center of Fig. 2(b). As opposed to the first epitaxial component, no additional low index plane alignments are identified in this case. Note that the ScSi(040) and ScSi(002) pole figures were also collected and are consistent with this analysis. Comparing XRD peak intensities, it is suggested that the *Epi 1* component is predominantly present in the material, i.e., most grains are oriented according to the *Epi 1* conditions.

The pole figure analysis reveals that the orth-ScSi grains have two different orientations. This is confirmed by cross-sectional TEM inspections (Fig. 3). Figure 3(a) shows a large-scale bright-field (BF) TEM image of the contact stack after the 420 °C to 20 min anneal. The orth-ScSi layer is polycrystalline. Two distinct regions can be observed: region 2, containing small (≲5 nm) nano-twinned grains, and region 1, containing large (≳20 nm) grains that are horizontally and vertically aligned with the substrate. The orientation of the ScSi grains in these two regions is further investigated by applying fast Fourier transformations (FFT) on high-resolution (HR) TEM images in Figs. 3(b)–3(d). Figure 3(b) shows multiple nano-twinned grains. As a result of the small size of the individual grains, a strong streaking effect can be observed in the FFT. In between the nano-twinned regions, some larger grains can be observed [Fig. 3(c)]. These grains are oriented according to the *Epi 1* texture component. Comparing Figs. 3(b) and 3(c) evidences that the nano-twinned

12 June 2026 12:02:48

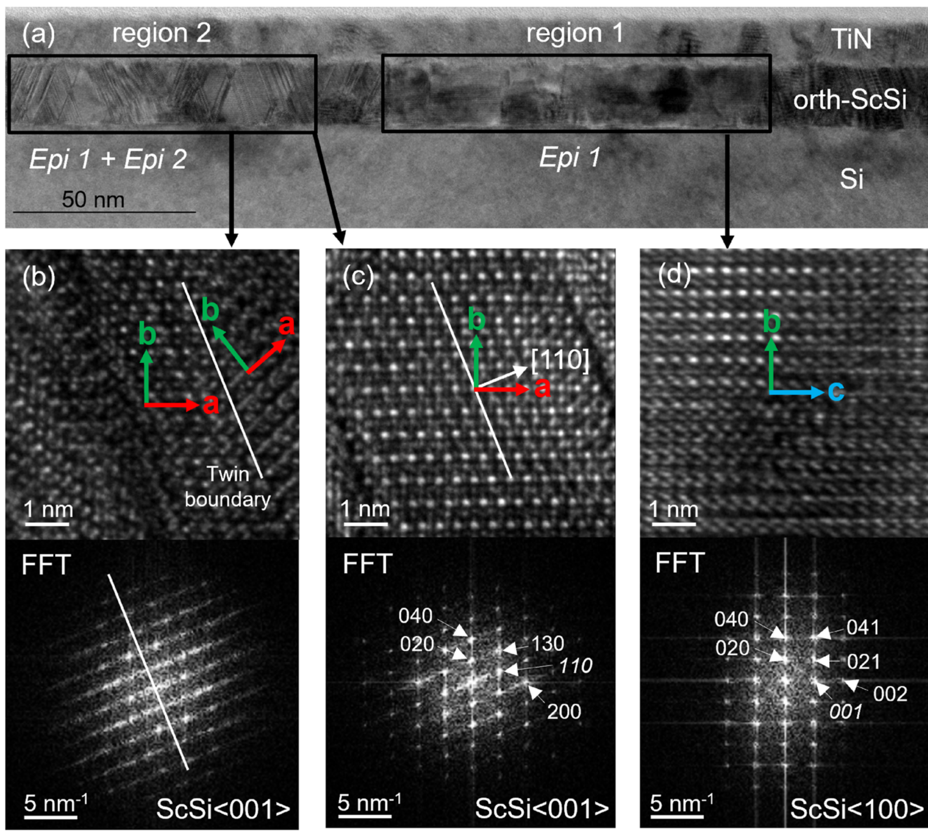

FIG. 3. (a) Large-scale BF-TEM image of a 10 nm TiN/15 nm Sc/Si(001) contact stack after 420 °C to 20 min anneal. HR-TEM images and corresponding FFTs taken in region 2 [(b) and (c)] and in region 1 (d). The FFT patterns are indexed using orthorhombic ScSi oriented along the indicated zone axis. The FFT spots indexed in italic correspond to kinematically forbidden diffraction spots.

© Author(s) 2026

grains correspond to *Epi 1* ScSi and *Epi 2* ScSi with their twin boundary along the (110) plane of the *Epi 1* grain. Indeed, the mirror image of *Epi 1* ScSi across the (110) plane (equivalent to a rotation of 44° about its **c** axis) results in the *Epi 2* orientation as determined by the pole figure analysis. The ScSi grain shown in Fig. 3(d) also corresponds to *Epi 1*. However, its in-plane component is rotated 90° about the **b** axis compared to Fig. 3(c).

C. Crystalline defects at the ScSi/Si interface

Figure 4(a) shows a HRTEM of the ScSi/Si interface for a ScSi grain oriented according to *Epi 1* [Fig. 3(d)]. The corresponding FFT image, including both ScSi and Si, shown in Fig. 4(b) reveals the lattice mismatch between ScSi(002) and Si(220). The alignment between these planes is visualized in the ScSi(002)/Si(220)-filtered inverse FFT shown in Fig. 4(c). The planes are epitaxially aligned across the contact interface. However, there is a misfit dislocation at the ScSi/Si interface every 23rd plane due to the large mismatch between the ScSi(002) and Si(220) interplanar spacings (Δd = 0.086 Å, corresponding to a lattice mismatch of −4.5%[33]). This domain-matching epitaxy[24] results in a nearly defect free silicide but a defective interface. In addition to the ScSi(002)//Si(220) alignment, the *Epi 1* oriented ScSi grains are also aligned along the **a** axis with the substrate: ScSi(200)//Si(220). However, despite a similar lattice mismatch (+4.2%), the grain size along the **a** axis is significantly smaller due to the presence of twin defects, i.e., the *Epi 2* grains. The resulting small grain size ($\lesssim$5 nm) and high defect density (up to ~1 defect/nm) are expected to be detrimental for contact applications. Note that this contrast in grain size is in agreement with the XRD peak intensities (Fig. 2) being significantly lower for the *Epi*

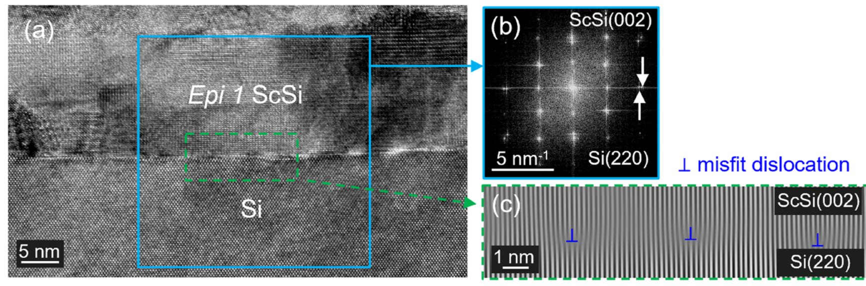

FIG. 4. (a) HRTEM image of ScSi/Si(001), oriented according to *Epi 1* [Fig. 3(d)]. (b) FFT image extracted from the ScSi/Si(001) interface. The high intensity spots corresponding to the ScSi(002) and Si(220) planes are indicated by arrows. (c) Corresponding ScSi(002)/Si(220) FFT filtered image showing the presence of misfit dislocations near the interface.

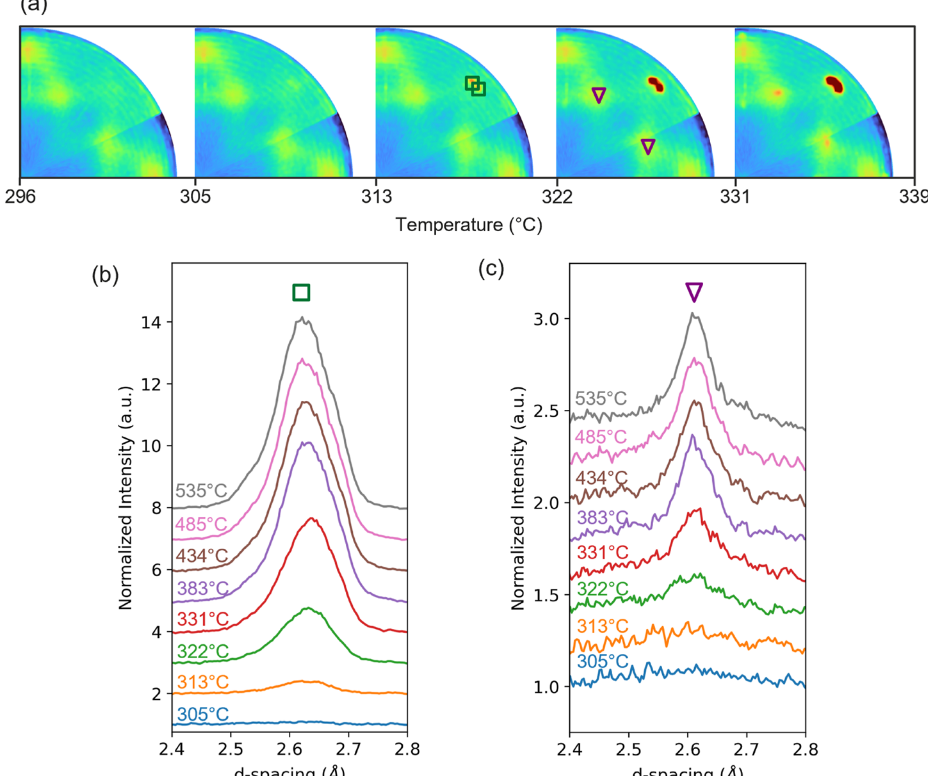

FIG. 5. (a) Series of *in situ* ScSi(111) XRD pole figures (for ϕ from 0° to 90°) from 10 nm TiN/15 nm Sc/Si(001) measured during a slow temperature ramp of 1 °C/min. The peak positions corresponding to the *Epi 1* and *Epi 2* texture component are indicated by square (□) and triangle (▽) symbols, respectively. Selection of XRD patterns corresponding to (b) *Epi 1* and (c) *Epi 2* peaks of the ScSi(111) reflection measured between 305 and 587 °C. The indicated temperatures are the starting values of the temperature interval at which the measurement is done. Note that the backgrounds have been artificially offset between successive measurements to improve readability.

12 June 2026 12:02:48

© Author(s) 2026

2 component compared to the *Epi 1* component. This anisotropic crystallization during the phase transition of a-ScSi to orth-ScSi is investigated further in Sec. III D.

D. Anisotropic crystallization of ScSi

In situ XRD pole figures are acquired on pristine samples to understand the formation of the two different epitaxial texture components. The phase transition from a-ScSi to orth-ScSi is evidenced in Fig. 5(a), which shows the temperature evolution of the ScSi(111) pole figure between 296 and 339 °C. To compare the formation temperature between the *Epi 1* and the *Epi 2* ScSi grains, the intensity on the pole figure is plotted as a function of the d-spacing [Figs. 5(b) and 5(c)]. To do so, the intensity is averaged over the ϕ and χ intervals corresponding to the position of the targeted peak in the pole volume. In Fig. 5(b), this is done for $\phi \in [40, 42]^\circ$ and $\chi \in [74, 76]^\circ$, which corresponds to the *Epi 1* ScSi(111) peak indicated in Fig. 5(a). Similarly, Fig. 5(c) corresponds to $\phi \in [67, 69]^\circ$ and $\chi \in [50, 52]^\circ$, which yields the *Epi 2* ScSi(111) peak. Comparing Figs. 5(b) and 5(c), one observes that in the temperature interval $[313, 322]^\circ$C, *Epi 1* ScSi starts to form, while this is not the case for *Epi 2* ScSi. This suggests that at the initial stages of orth-ScSi crystallization, the crystalline grains are exclusively oriented according to *Epi 1*.

To validate this result, cross-sectional TEM inspections are performed on a sample exposed to the 320 °C quenched anneal (Fig. 6). A large-scale BF-TEM image of this sample is shown in Fig. 6(a). Whereas the majority of the silicide is amorphous, nucleation of orth-ScSi at the interface with the Si substrate is evidenced in some areas. This nucleation appears to be strongly non-uniform, varying between ~20 and 40 nuclei per μm of interface (based on the inspection of four different regions across the TEM lamella[34]). The crystallinity and orientation of these nuclei are investigated by HR-TEM [Fig. 6(b)]. FFT analysis confirms that the nuclei consist of orth-ScSi [Fig. 6(c)]. Furthermore, it confirms that the orth-ScSi nucleus is oriented according to Fig. 3(d), i.e., *Epi 1* with a ScSi(010)//Si(001) out-of-plane and ScSi(001)//Si(100) in-plane orientation. Within the nuclei, no twin defects are observed in the various BF-TEM images [Fig. 6(a)], suggesting that all nuclei present during the initial stages of the orth-ScSi crystallization share this orientation, in agreement with the *in situ* pole figure analysis (Fig. 5).

The proposed reaction mechanisms are schematically depicted in Fig. 7. The silicide is fully amorphous prior to orth-ScSi formation. At the stage of initial crystallization, orth-ScSi nuclei are formed at the interface with Si. These nuclei are oriented exclusively according to the *Epi 1* texture component, i.e., aligned with the **b** axis out-of-plane and **a** and **c** axes in-plane, parallel to Si⟨110⟩ at $\chi = 90^\circ$ [Fig. 7(a)]. Further crystallization of ScSi occurs in an anisotropic manner. When viewed from the ScSi⟨100⟩ zone axis [Fig. 7(b)], the *Epi 1* grains oriented with **c** axis in-plane grow in a nearly defect free manner, resulting in large domain-matched epitaxial grains.[24] As a result of the lattice mismatch between ScSi and Si, there is a misfit dislocation at the ScSi/Si interface every 23rd plane [Fig. 7(b)]. For

12 June 2026 12:02:48

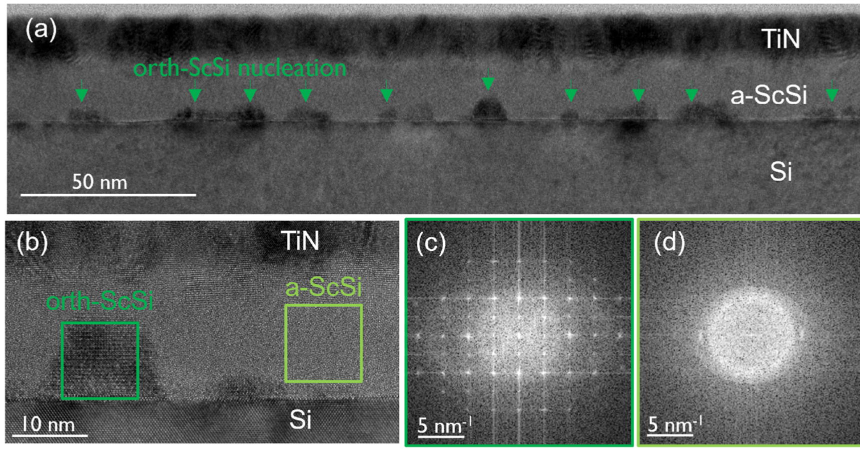

FIG. 6. (a) Large-scale BF-TEM image of a 10 nm TiN/15 nm Sc/Si(001) contact stack after a 320 °C quenched anneal. The arrows indicate the nucleation of orthorhombic ScSi at the interface with Si. (b) Corresponding HR-TEM image, highlighting an orthorhombic ScSi nucleus. FFTs extracted from the (c) orthorhombic ScSi nucleus and (d) amorphous ScSi.

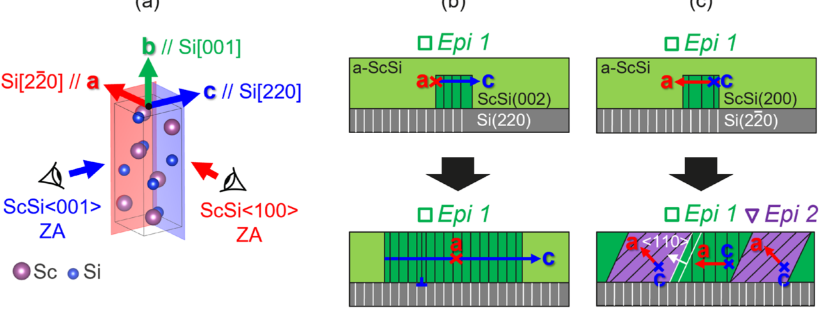

FIG. 7. (a) Orthorhombic ScSi unit cell oriented according to *Epi 1*. The ScSi⟨100⟩ and ScSi⟨001⟩ zone axes (ZA) are indicated. Schematic depiction of orthorhombic ScSi formation from amorphous ScSi viewed from the (b) ScSi⟨100⟩ and (c) ScSi⟨001⟩ zone axes, respectively.

© Author(s) 2026

in-plane growth along the **a** axis, the grain size is limited and twin defects are generated [Fig. 7(c)]. *Epi 1* grains are terminated by ⟨110⟩ facets, which act as twin planes. Mirroring the *Epi 1* grains across these planes results in the *Epi 2* orientation. Consequently, these *Epi 2* grains maintain the ScSi(001)//Si(110) in-plane alignment but are rotated out-of-plane compared to the *Epi 1* orientation.

IV. DISCUSSION

Silicide formation in metal/Si diffusion couples is known to occur through solid-state reactions that are governed by (long range) solid-state diffusion and nucleation. The connection between nucleation and silicide texture is well understood and can be explained on the basis of the classical nucleation theory.[35] The influence of diffusion processes during solid state reactions, on the other hand, is far from understood.[21,36]

Maas *et al.*[37] have reported on texturing caused by anisotropic diffusivity in silicides and germanides with the orthorhombic FeB structure. FeB has chains of B atoms along the [010] direction. The diffusion of B atoms takes place preferentially along these chains, resulting in highly anisotropic diffusion and a (010) out-of-plane texture. Given the similarity in crystal structure between orthorhombic ScSi (Cmcm space group) and FeB (Pnma space group), one might expect such anisotropic diffusion to also play a role. To clarify the role of (long range) diffusion in the a-ScSi to orth-ScSi phase transition, additional investigations are needed into the formation and properties of the former phase. In particular, the difference in composition between a-ScSi and orth-ScSi is key to understand the kinetics during this crystallization. Contrary to NiSi, for which the metal is the dominant diffusing species,[36] the formation of a-ScSi is driven by Si diffusion.[22] The kinetics of this diffusion-controlled process will be studied in a future work.

Orthorhombic NiSi has four axiotaxial and three epitaxial texture components when formed on Si(001).[38] ScSi, on the other hand, has a relatively simple texture constituting only two epitaxial components. Despite the lack of axiotaxy, the results suggest a preference for the system to align the ScSi(001) planes with the Si(110) substrate planes, as both texture components satisfy this condition. The following discussion focuses on explaining the observed texture components using the classical nucleation theory. In addition, it is shown that the formation of the twin defects is not linked to thermal stress that might arise due to a mismatch in the coefficient of thermal expansion (CTE) between the silicide and the substrate. Instead, it is hypothesized that this is linked to the low interface energy at the {110} twin boundary of *Epi 1* and *Epi 2* ScSi grains.

A. Texture selection during the nucleation of ScSi

The formation of a new phase during a solid-state reaction starts with the nucleation of very small nuclei of the new phase at the interface between the preceding phase and the substrate.[21] For the Sc/Si diffusion couple, the formation of orth-ScSi is preceded by the formation of a-ScSi. Upon further annealing, orth-ScSi crystallizes at the interface with Si. Consequently, the orientation of the new grains and, thus, the texture of the film will be determined at the interface between the nuclei of the new phase and the substrate.[21] From classical nucleation theory, it is known that the nucleation of a new phase is limited by the surface energy cost needed to form that phase. This energy cost can be minimized by forming a two-dimensional periodic interface structure, i.e., an epitaxial texture.[21] In agreement with the results of Voronov *et al.*, EDS suggests that the composition of a-ScSi is close to the one of orth-ScSi (see supplementary material). In such a case, the transformation of a-ScSi to orth-ScSi involves only a local reorganization of the atoms (i.e., a limited amount of new chemical bonds are created). The corresponding enthalpy change is expected to be low. Hence, the contribution of the interface energy becomes dominant and the preferential grain orientation has a high impact on the nucleation barrier. As a result, the formed phases are expected to be strongly textured, which explains the appearance of a single texture component at this stage of orth-ScSi formation.

B. Formation of twin defects during further orthorhombic ScSi crystallization

Upon further crystallization of the orth-ScSi phase, twin defects are formed [Fig. 3(b)]. A mismatch in CTE between a thin film and a single crystalline substrate can cause the formation of twin defects as a stress relief mechanism.[39] Detavernier *et al.*[40] showed that NiSi has an extremely anisotropic CTE that is much larger than the one of Si (up to 40×10^{-6}/°C for NiSi compared to 2.6×10^{-6}/°C for Si). This begs the question if a CTE mismatch between ScSi and Si could cause the formation of the observed defects. This has been investigated by annealing 10 nm TiN/15 nm Sc/Si(001) stacks at a constant temperature of 320 °C, i.e., the temperature at which the nucleation of the *Epi 1* orth-ScSi starts. The results of this are shown in the supplementary material. In this case, the full phase transition from a-ScSi to orth-ScSi occurs at a constant temperature, yet the final texture of the orth-ScSi film remains the same. This proves that the formation of the *Epi 2* grains is not the result of thermal stress arising from a mismatch in the CTE between the substrate and the silicide. From Sec. IV A, it is clear that the *Epi 1* orientation gives rise to the lowest interface energy at the ScSi/Si(001) interface. The interface energy between *Epi 2* ScSi and Si(001) should, therefore, be comparatively large. This is consistent with the narrow and elongated shape of the *Epi 2* grains, i.e., the area spanning their interface with Si is relatively limited. This indicates that the formation of the *Epi 2* ScSi grains is not driven by the interface energy between ScSi and Si (as is the case for the *Epi 1* grains). Instead, ScSi{110} twin boundaries form a low energy interface between different ScSi grains and are, therefore, the driving force for the crystallization of this second set of grains. Indeed, the formation of {110} twins is commonly reported to occur in orthorhombic crystals (referred to as the "{110} twin law").[41–43] In this case, the twin domains are transformed into one-another by reflection across a {110} plane, which preserves the orientation of the **c** axis. Since *Epi 1* ScSi is aligned with its **c** axis parallel to Si(110), the twinned domain will also satisfy this alignment. As a result, both the *Epi 1* and the *Epi 2* ScSi grains exhibit the ScSi(001)//Si(110) in-plane alignment. This shows that this plane alignment is not linked to an axiotaxial texturing, i.e., it is not the result of a matching of the projected d-spacings at the interface between the film and the substrate. Indeed, given the large lattice mismatch between ScSi(002) and Si(220) of −4.5% (which is the same for the mismatch in projected d-spacing), axiotaxy would not be expected in such a case.[44] The driving force for the presence (or absence) of this ScSi(001)//Si(110) preferential alignment will be

12 June 2026 12:02:48

© Author(s) 2026

further addressed in a follow-up study by comparing the texture of ScSi on Si(001), (110), and (111) substrates.

V. CONCLUSIONS

The formation and crystalline properties of orthorhombic ScSi thin films grown by sputter deposition of 15 nm of Sc on Si(001) have been investigated. The formation of orthorhombic ScSi is preceded by a solid state amorphization reaction between the as-deposited Sc and Si. This reaction results in a complete silicidation of the Sc layer, forming a fully amorphous a-ScSi layer. Upon further annealing, orthorhombic ScSi nuclei form at the interface with Si at ~320 °C. At this stage of the solid state reaction, orthorhombic ScSi formation is strongly driven by interface energy minimization, resulting in a singular epitaxial orientation of the ScSi nuclei with **a** and **c** axes oriented in-plane, parallel to the Si⟨110⟩ directions parallel to the interface. As a result, it can be concluded that this orientation exhibits the lowest interfacial energy with the Si(001) substrate.

At higher temperatures, further crystallization occurs anisotropically. Along the **c** axis, the epitaxial orientation is maintained, resulting in large (≳20 nm) grains with a minimal defectivity of one misfit every ~4.4 nm due to the lattice mismatch between the silicide and the substrate. However, along the **a** axis, twin defects are formed, resulting in a second set of epitaxially oriented grains with a significantly smaller grain size (≲5 nm). In light of electrical contact applications, the formation of this second set of grains is associated with a high twin defect density up to ~1 defect/nm and should, therefore, be avoided. A slow isothermal crystallization of the orthorhombic phase at 320 °C fails to prevent the twin defect formation. Consequently, it is hypothesized that this second set of grains is formed due to the favorable interface energy between ScSi grains at their {110} twin boundary as opposed to due to thermal stress.

SUPPLEMENTARY MATERIAL

The supplementary material discusses the EDS analysis results complementary to the cross-sectional TEM measurements shown in Figs. 3, 4, and 6 (S1) as well as the crystallization of orthorhombic ScSi during an isothermal anneal at 320 °C (S2). In addition, it includes a graphical representation of all possible orthorhombic ScSi orientations when imaged in cross section along the Si⟨110⟩ zone axis (S3).

ACKNOWLEDGMENTS

This work has been enabled in part by the NanoIC pilot line. The acquisition and operation are jointly funded by the Chips Joint Undertaking, through the European Union's Digital Europe (Grant No. 101183266) and Horizon Europe programs (Grant No. 101183277), as well as by the participating states Belgium (Flanders), France, Germany, Finland, Ireland, and Romania. For more information, visit nanoic-project.eu. Views and opinions expressed are, however, those of the author(s) only and do not necessarily reflect those of the European Union or Chips Joint Undertaking. Neither the European Union nor the granting authority can be held responsible for them. Elettra Sincrotrone Trieste is acknowledged for beamtime allocation on the MCX beamline (Proposal No. 20230227). The excellent support of beamline responsible J. Plaisier is acknowledged. Soleil synchrotron is acknowledged for beamtime allocation on the DiffAbs beamline (Proposal No. 20240142). The excellent support of beamline scientist C. Mocuta is acknowledged. The authors thank A. Akula and D. Schippers for assisting the measurements. In the supplementary material, results obtained at the ESRF DUBBLE BM26 beamline are included. The authors acknowledge the ESRF for beamtime allocation under Proposal No. A26-2-1005. Beamline scientist M. Rosenthal is acknowledged for his excellent support. The authors thank T. Dursap for assisting the measurements.

AUTHOR DECLARATIONS

Conflict of Interest

The authors have no conflicts to disclose.

Author Contributions

Bert Pollefliet: Conceptualization (lead); Data curation (lead); Formal analysis (lead); Investigation (equal); Methodology (lead); Resources (equal); Visualization (lead); Writing – original draft (lead); Writing – review & editing (equal). **Clement Porret**: Conceptualization (equal); Investigation (equal); Resources (lead); Supervision (equal); Writing – review & editing (equal). **Jean-Luc Everaert**: Data curation (supporting); Investigation (supporting). **Kiroubanand Sankaran**: Investigation (supporting). **Olivier Richard**: Data curation (equal); Investigation (equal); Writing – review & editing (supporting). **Han Han**: Data curation (equal); Investigation (equal); Writing – review & editing (supporting). **Roger Loo**: Conceptualization (equal); Supervision (equal); Writing – review & editing (equal). **Christophe Detavernier**: Data curation (supporting); Formal analysis (supporting); Supervision (equal); Writing – review & editing (equal). **André Vantomme**: Conceptualization (equal); Supervision (equal); Writing – review & editing (equal). **Clement Merckling**: Conceptualization (equal); Supervision (equal); Writing – review & editing (equal).

DATA AVAILABILITY

The data that support the findings of this study are available from the corresponding author upon reasonable request.

REFERENCES

[1] G. Yeric, in *IEEE International Electron Devices Meeting (IEDM)* (IEEE, 2015), p. 1.1.1.

[2] H. Yu, M. Schaekers, J.-L. Everaert, N. Horiguchi, K. De Meyer, and N. Collaert, MRS Adv. **7**, 1369 (2022).

[3] D. A. Yarekha, G. Larrieu, E. Dubois, S. Godey, X. Wallart, C. Soyer, D. Remiens, N. Reckinger, X. Tang, A. Laszcz, and J. Ratajczak, in Journées Nationales sur les Technologies Emergentes en Micro-Nanofabrication (JNTE 08), 2008.

[4] K. N. Tu, R. D. Thompson, and B. Y. Tsaur, Appl. Phys. Lett. **38**, 626 (1981).

[5] H. Yu, L.-L. Wang, M. Schaekers, J.-L. Everaert, Y.-L. Jiang, D. Mocuta *et al.*, IEEE Electron Device Lett. **38**(7), 843 (2017).

[6] W. Huang, G.-P. Ru, C. Detavernier, R. L. Van Meirhaeghe, Y.-L. Jiang, X.-P. Qu, and B.-Z. Li, Microelectron. Eng. **85**, 131 (2008).

12 June 2026 12:02:48

© Author(s) 2026

[7]S. M. Hogg, A. Vantomme, and M. F. Wu, J. Appl. Phys. **91**, 3664 (2002).
[8]S. M. Hogg, A. Vantomme, M. F. Wu, and G. Langouche, Microelectron. Eng. **50**, 211 (2000).
[9]F. M. d'Heurle, M. O. Aboelfotoh, F. Pesavento, and C. S. Petersson, Appl. Surf. Sci. **53**, 237 (1991).
[10]C. Porret, J.-L. Everaert, M. Schaekers, L.-A. Ragnarsson, A. Hikavyy, E. Rosseel, G. Rengo, R. Loo, R. Khazaka, M. Givens, X. Piao, S. Mertens, N. Heylen, H. Mertens, C. Toledo de Carvalho Cavalcante, G. Sterckx, S. Brus, A. Nalin Mehta, M. Korytov, D. Batuk, P. Favia, R. Langer, G. Pourtois, J. Swerts, E. Dentoni Litta, and N. Horiguchi, in *IEEE International Electron Devices Meeting (IEDM)* (IEEE, 2022), p. 34.1.1.
[11]X. Sun, J. Xu, J. Gao, J. Liu, Y. He, X. Chen, M. Kong, Y. Li, J. Li, W. Wang, T. Ye, and J. Luo, J. Mater. Sci.: Mater. Electron. **34**, 1239 (2023).
[12]O. Thomas, C. S. Peterson, and F. M. d'Heurle, Appl. Surf. Sci. **53**, 138 (1991).
[13]H. Jeon, G. Yoon, and R. J. Nemanich, Thin Solid Films **299**(1–2), 178 (1997).
[14]P. Tiwari, R. Singh, and J. Narayan, Philos. Mag. B **68**(3), 413 (1993).
[15]B. Meyer, U. Gottlieb, O. Laborde, H. Yang, J. C. Lasjaunias, A. Sulpice, and R. Madar, Microelectron. Eng. **37–38**, 523 (1997).
[16]M. Fazio, L. Yang, A. Markosyan, R. Bassiri, M. M. Fejer, and C. S. Menoni, Appl. Opt. **59**(5), A106 (2020).
[17]J. W. Hennek, J. Smith, A. Yan, M.-G. Kim, W. Zhao, V. P. Dravid, A. Facchetti, and T. J. Marks, J. Am. Chem. Soc. **135**, 10729 (2013).
[18]A. Dabral, G. Pourtois, K. Sankaran, W. Magnus, H. Yu, A. de Jamblinne de Meux, A. K. A. Lu, S. Clima, K. Stokbro, M. Schaekers *et al.*, ECS J. Solid State Sci. Technol. **7**, N73 (2018).
[19]B. Pollefliet, C. Porret, J.-L. Everaert, K. Sankaran, X. Piao, E. Rosseel, T. Conard, A. Impagnatiello, Y. Shimura, N. Horiguchi, R. Loo, A. Vantomme, and C. Merckling, Jpn. J. Appl. Phys. **63**, 02SP97 (2024).
[20]B. Pollefliet, C. Porret, J.-L. Everaert, K. Sankaran, X. Piao, E. Rosseel, T. Conard, A. Impagnatiello, Y. Shimura, A. Hikavyy, R. Loo, A. Vantomme, and C. Merckling, in *International Conference on Solid State Devices and Materials* (The Japan Society of Applied Physics, 2023), p. 289.
[21]B. De Schutter, K. De Keyser, C. Lavoie, and C. Detavernier, Appl. Phys. Rev. **3**, 031302 (2016).
[22]D. L. Voronov, E. N. Zubarev, V. V. Kondratenko, Y. P. Pershin, V. A. Sevryukova, and Y. A. Bugayev, Thin Solid Films **513**, 152 (2006).
[23]L. Chen, Mater. Sci. Eng. **R29**(5), 115 (2000).
[24]J. Deng, H. Li, K. Dong, R.-W. Li, Y. Peng, G. Ju, J. Hu, G. M. Chow, and J. Chen, Phys. Rev. Appl. **9**, 034023 (2018).
[25]J. R. Plaisier, L. Nodari, L. Gigli, E. P. Rebollo San Miguel, R. Bertoncello, and A. Lausi, Acta IMEKO **6**(3), 71 (2017).
[26]K. D. Keyser, "Texture of thin silicide and germanide films," Ph.D. dissertation (Department of Solid State Sciences, Ghent University, 2011).
[27]K. De Keyser, C. Detavernier, J. Jordan-Sweet, and C. Lavoie, Thin Solid Films **519**, 1277 (2010).
[28]C. Mocuta, M.-I. Richard, J. Fouet, S. Stanescu, A. Barbier, C. Guichet, O. Thomas, S. Hustache, A. V. Zozulya, and D. Thiaudière, J. Appl. Crystallogr. **46**, 1842 (2013).
[29]F. Geenen, "Formation and texture of thin film silicides," Ph.D. dissertation (Department of Solid State Sciences, Ghent University, 2017).
[30]V. Holzer, B. Schrode, J. Simbrunner, S. Hofer, L. Barba, R. Resel, and O. Werzer, Rev. Sci. Instrum. **93**, 063906 (2022).
[31]B. Pollefliet, C. Porret, C. Detavernier, J.-L. Everaert, K. Sankaran, E. Rosseel, R. Loo, A. Vantomme, and C. Merckling, in *International Conference on Solid State Devices and Materials* (The Japan Society of Applied Physics, 2024), p. 607.
[32]For a perfect ScSi(130)//Si(001) out-of-plane orientation, the ScSi(010) planes are tilted 39.5° out-of-plane which corresponds to the angle between ScSi(130) and ScSi(010).
[33]The lattice mismatch *lmm* between the d-spacing of o-ScSi and Si is calculated as: $lmm = \frac{d(ScSi)-d(Si)}{d(Si)}$.
[34]In these TEM inspections, nuclei larger than 3 nm are clearly visible and are included in this estimation.
[35]F. M. d'Heurle, J. Mater. Res. **3**(1), 167 (1988).
[36]K. van Stiphout, F. A. Geenen, N. M. Santos, S. M. C. Miranda, V. Joly, J. Demeulemeester, C. Detavernier, F. Kremer, L. M. C. Pereira, K. Temst, and A. Vantomme, J. Phys. D: Appl. Phys. **52**, 145301 (2019).
[37]J. H. Maas, G. F. Bastin, F. J. J. Van Loo, and R. Metselaar, J. Appl. Crystallogr. **17**, 103 (1984).
[38]C. Detavernier, J. Jordan-Sweet, and C. Lavoie, J. Appl. Phys. **103**, 113526 (2008).
[39]A. Bartasyte, V. Plausinaitiene, A. Abrutis, T. Murauskas, P. Boulet, S. Margueron, J. Gleize, S. Robert, V. Kubilius, and Z. Saltyte, Appl. Phys. Lett. **101**, 122902 (2012).
[40]C. Detavernier, C. Lavoie, and F. M. d'Heurle, J. Appl. Phys. **93**(5), 2510 (2003).
[41]P. N. Gavryushkin, A. Rečnik, N. Daneu, N. Sagatov, A. B. Belonoshko, Z. I. Popov, V. Ribić, and K. D. Litasov, Z. Kristallogr. - Cryst. Mater. **234**(2), 79 (2019).
[42]S. Parsons, Acta Crystallogr., Sect. D: Biol. Crystallogr. **59**, 1995 (2003).
[43]M. Nespolo and B. Souvignier, Crystallogr. Rev. **30**(2), 135 (2024).
[44]C. Detavernier, A. S. Özcan, J. Jordan-Sweet, E. A. Stach, J. Tersoff, F. M. Ross, and C. Lavoie, Nature **426**, 641 (2003).

12 June 2026 12:02:48

© Author(s) 2026